

Statistical Analysis of Equatorial Plasma Irregularities Retrieved From Swarm 2013–2019 Observations

Ercha Aa^{1,2} , Shasha Zou¹ , and Siqing Liu³ 

¹Department of Climate and Space Sciences and Engineering, University of Michigan, Ann Arbor, MI, USA, ²Now at Haystack Observatory, Massachusetts Institute of Technology, Westford, MA, USA, ³National Space Science Center, Chinese Academy of Sciences, Beijing, China

Key Points:

- The postsunset EPI occurrence rate is positively correlated with solar activity, while the postmidnight EPI is negatively correlated with it
- The postsunset (postmidnight) EPIs are more prominent during the equinoxes (June solstice) over the American-Atlantic (African) sector
- The latitudinal variation of EPIs exhibits an asymmetric double-peak distribution pattern that prevails in the summer hemisphere

Correspondence to:

E. Aa,
aercha@mit.edu

Citation:

Aa, E., Zou, S., & Liu, S. (2020). Statistical analysis of equatorial plasma irregularities retrieved from Swarm 2013–2019 observations. *Journal of Geophysical Research: Space Physics*, 125, e2019JA027022. <https://doi.org/10.1029/2019JA027022>

Received 10 JUN 2019

Accepted 15 MAR 2020

Accepted article online 16 APR 2020

Abstract In this study, we present a statistical analysis of equatorial plasma irregularities (EPIs) by using in situ plasma density measurements of the Swarm constellation from December 2013 to December 2019. The occurrence patterns for both postsunset and postmidnight EPIs with respect to longitude, season, local time, latitude, solar activity, and geomagnetic activity level are investigated. The main findings are as follows: (1) The postsunset/postmidnight EPIs occurrence rates exhibit different longitudinal and seasonal dependence: The postsunset EPIs have the maximum occurrence rate over the American-Atlantic sectors during the December solstice and equinoxes, and the postmidnight EPIs have the maximum occurrence rate during the June solstice, especially over the African sector. (2) The postsunset EPIs occurrence rates have a positive correlation with solar activity, while the postmidnight EPIs are negatively correlated with it. (3) The latitudinal distribution of EPIs exhibits a double-peak structure around $\pm 5^\circ$ magnetic latitude with a more significant peak in the summer hemisphere. (4) The EPIs occurrence rate increases with increasing geomagnetic activity level. (5) The main controlling factors for the distribution of postsunset EPIs are the magnetic declination angle, equatorial vertical $E \times B$ drift, and thermospheric zonal wind. For the postmidnight EPIs, the main controlling factors are likely to be atmospheric gravity waves and equatorward thermospheric meridional wind associated with midnight temperature maximum.

1. Introduction

Equatorial plasma irregularities (EPIs) refer to irregular plasma density structures over the equatorial and low-latitude ionosphere, which can adversely affect the performance of navigation and communication systems and thus have been extensively investigated for decades. EPIs associated with equatorial plasma bubbles are generated by the Rayleigh-Taylor (R-T) instability in the bottomside ionosphere, and they can penetrate vertically through the topside ionosphere, extend to higher altitudes, and map to higher latitudes along the magnetic field lines (Fejer et al., 1999; Kelley et al., 1976; Ott, 1978; Tsunoda, 1980; Tsunoda et al., 1982). The morphology and evolution processes of EPIs have been widely studied by using multi-instrument measurements. For example, density irregularities are seen as airglow emission depletions in optical observations of ground-based all-sky imagers or space-based ultraviolet imagers (Aa et al., 2020; Comberiate & Paxton, 2010; Kelley et al., 2003; Kil, Heelis, et al., 2009; Makela & Kelley, 2003; Martinis et al., 2015), plume-like structures in radar backscatter measurements (Jin et al., 2018; Li et al., 2013; Woodman & La Hoz, 1976; Yokoyama & Fukao, 2006), range-type equatorial spread-F (ESF) echoes on ionograms (Abdu et al., 2003; Li et al., 2018), in situ plasma density depletions detected by Low-Earth Orbiting (LEO) satellite observations (Aa et al., 2018; Basu et al., 2001; Cherniak et al., 2019; Huang et al., 2007, 2012; Xiong et al., 2010, 2018; Zakharenkova et al., 2016), and total electron content (TEC) depletions derived from Global Navigation Satellite System (GNSS) measurements (Aa et al., 2019; Blanch et al., 2018; Cherniak & Zakharenkova, 2016; Ma & Maruyama, 2006; Katamzi-Joseph et al., 2017). Moreover, numerical models have also been used to study the triggering mechanisms of EPIs (e.g., Aveiro et al., 2012; Carter et al., 2016; Huba & Joyce, 2007; Huba et al., 2008; Krall et al., 2011; Retterer & Gentile, 2009; Yokoyama et al., 2014).

Statistical studies have been conducted to understand the occurrence probability of EPIs as a function of local time, latitude, longitude, season, solar cycle, and geomagnetic variation. Much has been done by using long-term continuous observations, such as ground-based GNSS receivers and space-based radio occultation measurements (Carter et al., 2013; Nishioka et al., 2008; Yu et al., 2018), measurements of retarding potential analyzer onboard Atmosphere Explorer-E (AE-E) satellite (Kil & Heelis, 1998), plasma density

detected by ion sensor onboard the Defense Meteorological Satellite Program (DMSP) (Burke, Gentile, et al., 2004; Burke, Huang, et al., 2004; Gentile et al., 2006; Huang et al., 2002), observations of the Ion Trap sensor onboard FORMASAT-1 satellite (Su et al., 2006, 2008; Kil, Paxton, et al., 2009), measurements of the Ion Velocity Meter (IVM) or Planar Langmuir Probe onboard the Communications/Navigation Outage Forecasting System (C/NOFS) satellite (Huang et al., 2014; Retterer & Roddy, 2014; Smith & Heelis, 2017; Yizengaw et al., 2013), flux-gate magnetometer measurements onboard CHAMP satellite (Lühr et al., 2014; Stolle et al., 2006), and electric field instrument (EFI) measurements onboard Swarm constellation (Rodríguez-Zuluaga et al., 2017; Wan et al., 2018; Xiong et al., 2016, 2018; Zakharenkova et al., 2016).

Although significant progress has been achieved through these statistical studies, characterization of the global temporal/spatial distribution of EPIs is still a challenging problem. Some important issues still need further investigation, including the following: (1) What are the differences and similarities of postsunset and postmidnight EPI occurrence rate and their major controlling factors? Many studies have found that the postsunset EPIs have higher occurrence rate in the Atlantic-African sectors and lower occurrence rate in the Indian-Pacific sectors and maximum occurrence rate is usually observed in the equinoxes and minimum occurrence rate is usually observed between May and August (e.g., Burke, Gentile, et al., 2004; Burke, Huang, et al., 2004; Huang et al., 2001, 2002; Gentile et al., 2006). These longitudinal and seasonal results were also confirmed by some other studies among which the conclusion is drawn by merging the evening and morning EPIs as a whole (e.g., Kil, Paxton, et al., 2009; Lühr et al., 2014; Stolle et al., 2006; Su et al., 2006, 2008). However, the formation mechanism of the postmidnight EPIs is still under debate, and only few statistical studies have been conducted to investigate the spatial and temporal distribution of postmidnight EPIs (Wan et al., 2018; Yizengaw et al., 2013). Both Yizengaw et al. (2013) and Wan et al. (2018) found that strong occurrence peak of postmidnight EPIs exists during June solstice predominantly in the African sector, which is quite different from the postsunset results. Thus, it is necessary to further study the differences/similarities of postsunset and postmidnight EPIs and investigate the possible factors that control their longitudinal and seasonal distribution. (2) How to interpret the seemingly conflicting observations of solar dependence on EPI occurrence rate? Some prior studies indicated that EPIs are more often detected during solar maximum and less during solar minimum (e.g., Carter et al., 2013; Huang et al., 2002; Stolle et al., 2006; Yu et al., 2018), while some other studies showed that the postmidnight EPIs have higher occurrence rate during low solar activity period (Makela & Miller, 2011; Smith & Heelis, 2017) and the African sector has larger occurrence rate and higher correlation with F10.7 than other sectors during solar minimum (Dao et al., 2011; Nishioka et al., 2008; Yizengaw et al., 2013). Thus, the role of solar activity in the occurrence of EPIs remains an open question and needs to be further studied.

Recently, Wan et al. (2018) conducted an interesting quiet time climatological study on the occurrence and amplitude of equatorial plasma depletions by using the Swarm constellation in situ electron density from 2013 to 2017. They found that the highest occurrence rate and the largest amplitudes of equatorial plasma depletions are rarely related with each other, and the occurrence rate of postmidnight is generally reduced compared to premidnight ones at most longitudes except for the African sector. In this study, we extended the work of Wan et al. (2018) to investigate in depth the statistical behavior of the occurrence rate of both postsunset and postmidnight EPIs as well as their dependence on solar and geomagnetic activity levels. The results were also derived from the Swarm in situ *Ne* measurements but covering a longer time period from December 2013 to December 2019, which basically covers the declining phase of Solar Cycle 24 with a full range of solar and geomagnetic activity levels. We specified the diurnal, seasonal, longitudinal, and latitudinal distribution patterns of both postsunset and postmidnight EPIs and discussed their similar/different driven mechanisms correspondingly based on the identified pattern. We also examined the solar and geomagnetic activity dependences of EPIs. We sought answers for the above-mentioned questions and achieved further insights into the spatial/temporal variability of EPIs. The rest of the paper is organized as follows: The data set and the processing method will be briefly introduced in section 2. The statistical results of EPIs will be given in section 3. The discussions and conclusions will be presented in sections 4 and 5, respectively.

2. Data and Method

The Swarm constellation consists of three satellites, which were launched into an approximately circular near-polar orbit ($\sim 88^\circ$) on 22 November 2013. Swarm A and Swarm C fly side by side at an altitude of 440–460 km, separated by about 1.4° in longitude. The third satellite, Swarm B, orbits the Earth at about

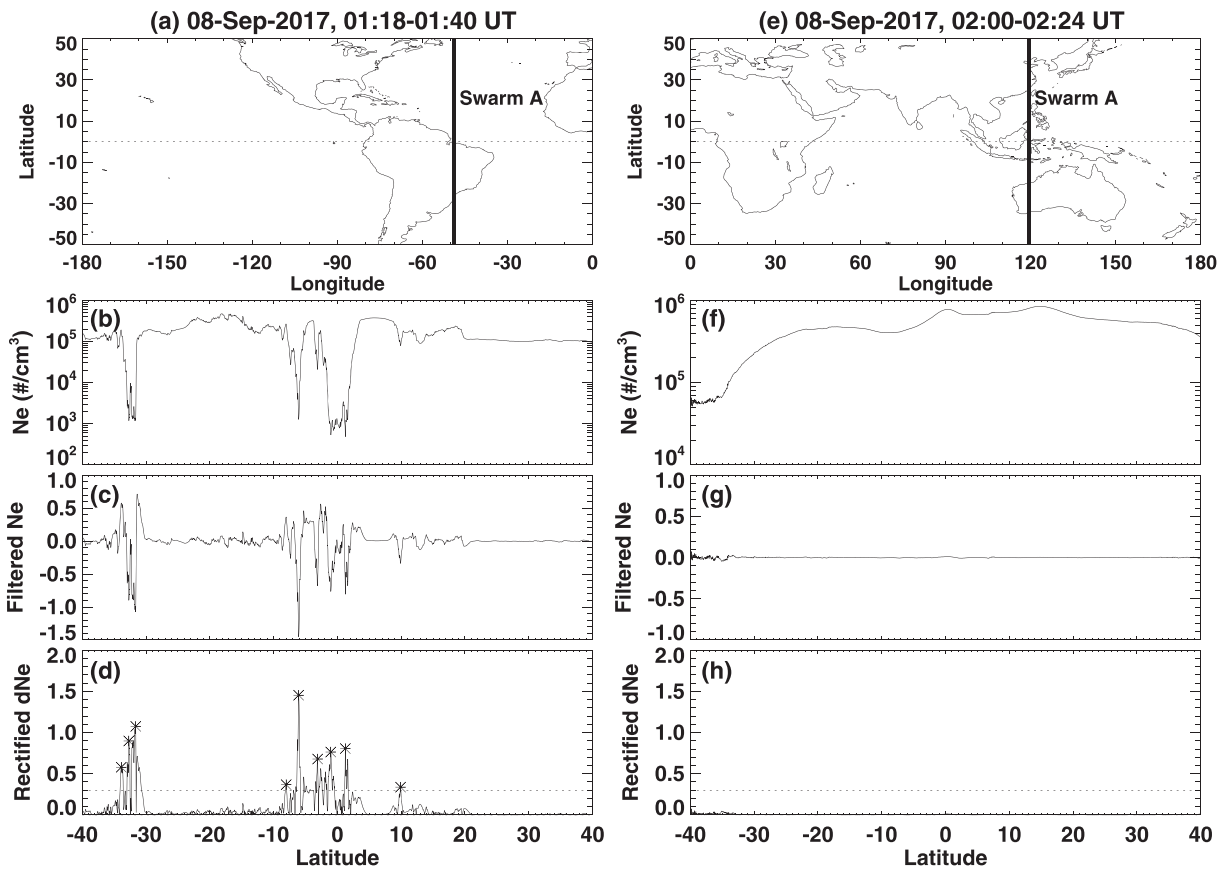


Figure 1. Example of EPIs measured by Swarm A satellite on 8 September 2017. (a) The global map with an orbit of Swarm A being superposed, (b) the corresponding N_e profile as a function of latitude in log scale, (c) high-pass filtered N_e , and (d) rectified residuals. (e–h) The same as (a)–(d) but for another orbit with no EPIs being detected. The detected EPIs are marked with asterisk. EPIs = equatorial plasma irregularities.

520 km with a higher inclination. This provides an opportunity to make a comparative analysis of ionospheric irregularities by using similar N_e measurements from identical instruments at different altitudinal/longitudinal sectors. Swarm has comprehensive payload elements: vector field magnetometer, absolute scalar magnetometer, electric field instrument, accelerometer, laser range reflector, and GPS receiver. One of the most relevant instruments onboard is the electric field instrument (EFI) that is capable of measuring the plasma density with a time resolution of 2 Hz, which affords an excellent opportunity to study the variability and distribution of plasma irregularities.

Different algorithms have been used for extracting the EPI events from the N_e measurements, and we use a similar method to that described by Xiong et al. (2016), Stolle et al. (2006), Wan et al. (2018), and references therein. First, the continuous time series of N_e profiles, after quality control flags were applied, were divided into orbital segments of equatorial crossing within a range of $\pm 40^\circ$ geomagnetic latitude. Then the log electron density of each orbital segment was high-pass filtered with a cutoff period of 40 s that corresponds to an along-track spatial scale of ~ 300 km. Subsequently, the filtered residual was rectified. Residual values exceeding a threshold were identified as the EPIs events. Since there is no generally accepted value of the threshold, after estimating the level of quiet time N_e variations and considering the previous references (e.g., Kil, Paxton, et al., 2009; Su et al., 2006; Xiong et al., 2016), the value of 0.3 was used in the current study as the threshold to identify irregularities. Besides, after implementing a sensitivity analysis, we found that a 30% fluctuation in the current threshold level will only lead to 5–7% variation in the statistical results; thus, the characteristics of EPIs could be obtained using this threshold. To illustrate the above-mentioned algorithm, Figure 1 shows an example of plasma irregularities measured by Swarm A on 8 September 2017. Figures 1a and 1b present satellite orbit and the corresponding latitudinal profile of the plasma density, respectively. Figures 1c and 1d display the high-pass filtered N_e and the rectified residuals, respectively. The rectified peak values, if larger than the threshold, were considered as significant EPI events

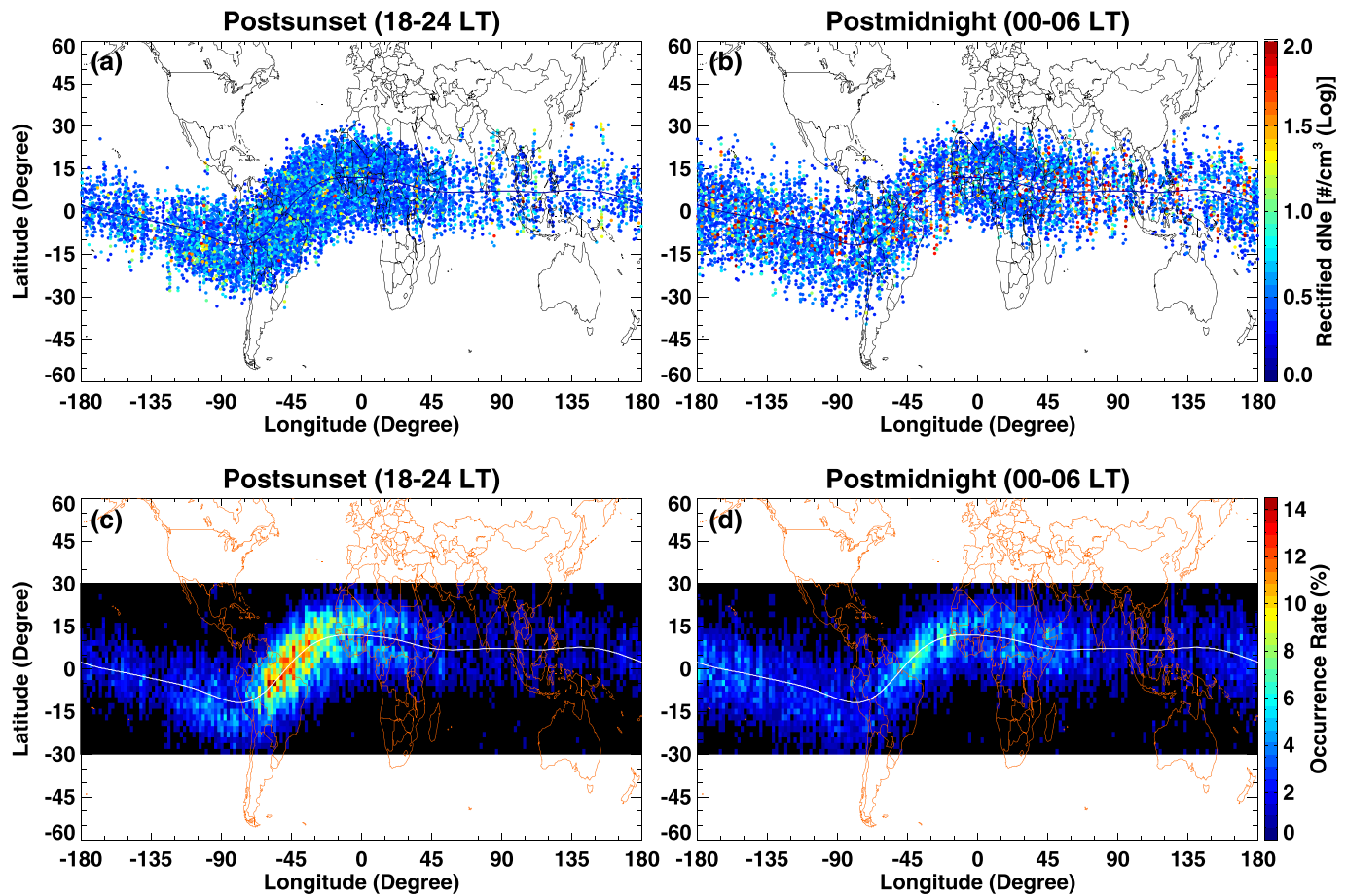


Figure 2. Global distribution of EPIs amplitudes during (a) postsunset and (b) postmidnight period. Global distribution of EPIs occurrence rate during (c) postsunset and (d) postmidnight period. The geomagnetic equator is also plotted. EPIs = equatorial plasma irregularities.

(marked with an asterisk). The right panels (Figures 1e–1h) show an example of orbit with no considerable plasma irregularities being detected.

3. Statistical Results

3.1. Longitudinal and Seasonal Distribution

With more than 20,000 EPI events identified using the approach described above, the global distribution of these events and their associated amplitudes are shown in the form of colored scatter points during postsunset (18–24 LT, Figure 2a) and postmidnight (0–6 LT, Figure 2b) period, respectively. Figures 2c and 2d display the gridded distribution of the occurrence rates for those two periods with a spatial resolution of $2^\circ \times 2^\circ$ in geographic coordinates. The occurrence rate is defined as the ratio of the number of the detected EPI events to the number of satellite crossings in each postsunset/postmidnight bin. It can be seen that most of the plasma irregularities are confined to within 30° of the geomagnetic equator. Moreover, in the postsunset sector, the distribution of irregularities has a much higher density and occurrence rate over the African, Atlantic, and South American sectors in longitudes between -60° and 30° , while relatively fewer irregularities are located over the Asian sector. In the postmidnight sector, the Atlantic and African sectors still have higher occurrence rates; however, the Asian and Pacific sectors have more EPIs events than the postsunset case, and the amplitude of irregularities can be substantial (i.e., 2 orders of magnitudes change) over these sectors. This implies that the highest occurrence rate does not always coincide with the largest depletion amplitude, which is similar to the results in Wan et al. (2018).

To further specify the seasonal variation of the plasma irregularities, Figure 3 shows the global distribution and the longitudinal distribution of the occurrence rate of EPIs for all seasons, the December solstice, the March/September equinoxes, and the June solstice. The gridded occurrence rates shown in Figures 3a, 3c,

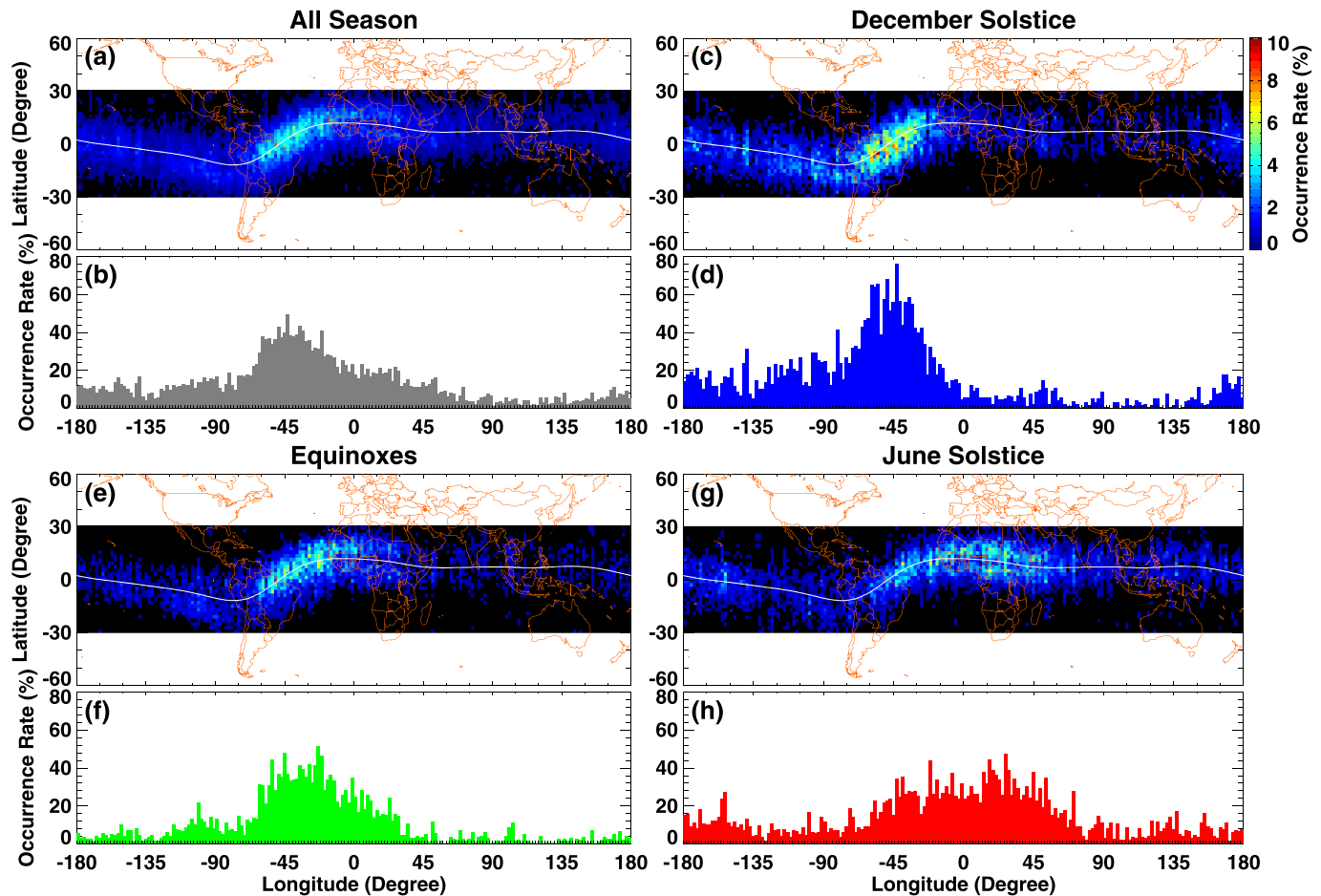


Figure 3. The gridded and longitudinal distribution of the EPI occurrence rate for all seasons (a and b), the December solstice (c and d), the spring/autumn equinoxes (e and f), and the June solstice (g and h). The thick white curve represents the geomagnetic equator. EPI = equatorial plasma irregularity.

3e, and 3g were calculated as the ratio of the detected EPI numbers to the satellite crossing counts in each bin. The 1-D occurrence rate shown in Figures 3b, 3d, 3f, and 3h is calculated as the ratio of the number of orbits in which EPIs were detected divided to the total number of orbits in each longitudinal band. The all-season result of Figure 3a exhibits that the occurrence rate has much higher values over the African-Atlantic-South American regions, which has a similar longitudinal and latitudinal distribution pattern with those indicated in Figure 2. However, there are distinct variations in the distribution pattern of different seasons. Near the December solstice, the density irregularity is more frequently detected over the South American sector (60–30°W) with the occurrence rate ranging from 40–80%. For the March/September equinoxes, the longitudinal preference of EPIs extends to the Atlantic and west African sectors (45°W to 15°E), while the occurrence rate over these region reduces to 30–50%. As for the June solstice, the distribution is relatively even with broader longitude coverage, and the peak of occurrence rate shifts to the African sector.

Figures 4a and 4b show the seasonal-longitudinal distribution of the occurrence rate of EPIs during post-sunset and postmidnight periods, respectively. The resolution is 10° in longitude and half a month in time, and the occurrence rate is normalized by the number of satellite crossings as shown in Figures 4c and 4d. For the postsunset period, the monthly occurrence pattern shows larger values near the two equinoxes: one in February–March and another one in October–November. In both season there is a clear longitudinal preference for the Atlantic-American sector. Moreover, the postsunset occurrence rate of EPIs was lower during the periods of May–September; the irregularity signature is severely suppressed in the Atlantic-American sector but mainly confined within the African and Pacific regions, which is consistent with those indicated in Stolle et al. (2006). On the other hand, during the postmidnight period, the distribution pattern exhibits the opposite feature: The region of high occurrence rate shifts longitudinally from the Atlantic to the African

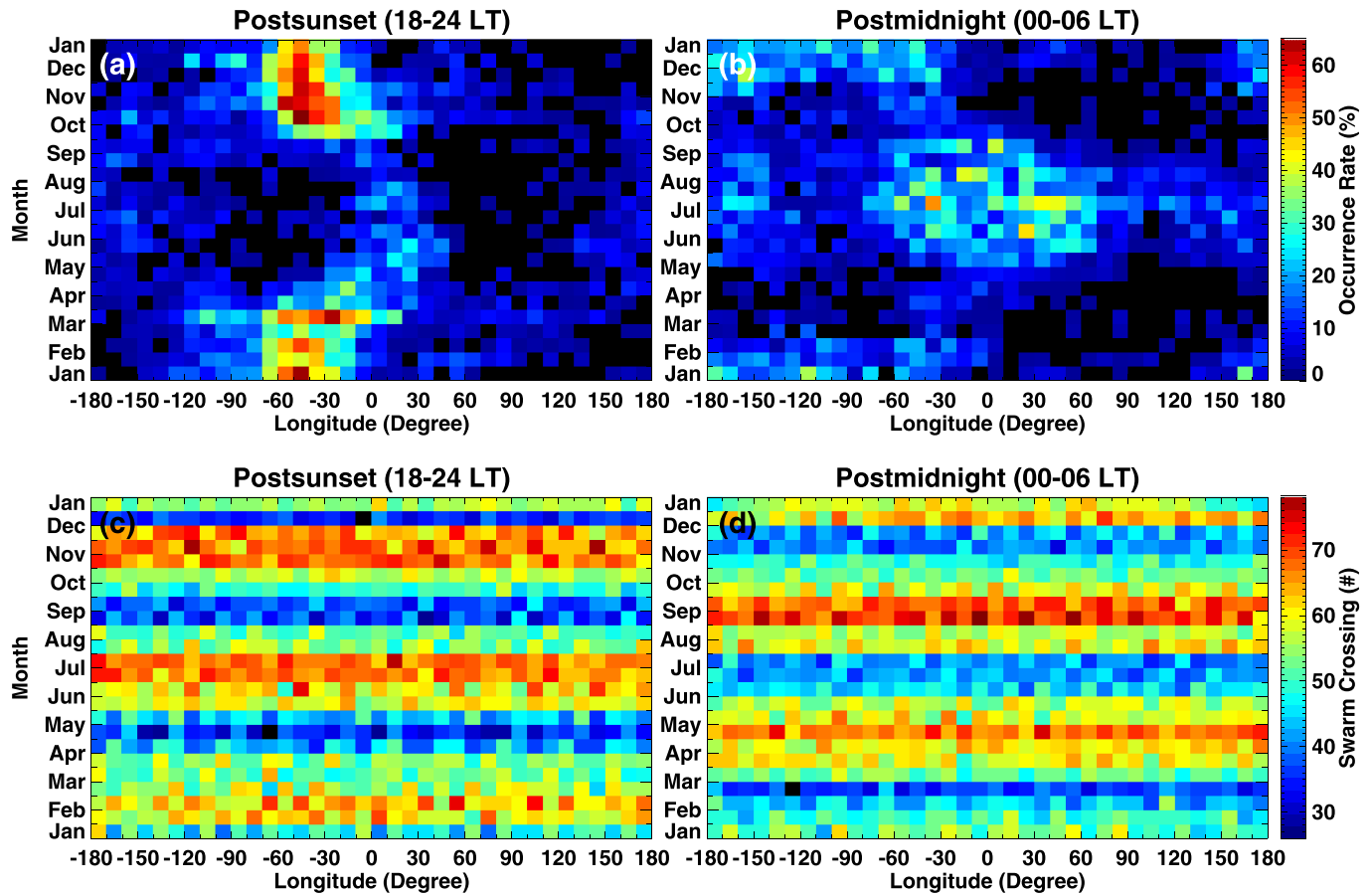


Figure 4. Seasonal-longitudinal distribution of the EPI occurrence rate (a and b) and the Swarm crossing counts (c and d) during the postsunset and postmidnight periods, respectively. EPI = equatorial plasma irregularity.

sector around June solstice and to the Pacific sector around the December solstice, while the occurrence rate around the equinoxes is substantially reduced. One thing worth noting is that the Swarm constellation does not have equal coverage of all spatial-temporal bins. For example, the postsunset period has less data availability around May/August and more availability around February, June, and November. The situation for the postmidnight is similar but shifted by a couple of months. This could make the above-mentioned statistical results have different uncertainty variations. Thus, the error bars showing possible biases due to the uneven data coverage are introduced here, which can be calculated as follows:

$$\sigma = \sqrt{\frac{f \times (1 - f)}{N - 1}}, \quad (1)$$

where σ is the uncertainty, f is the occurrence rate, and N is the total number of satellite pass for each given bin.

Figure 5 shows the monthly variation of the occurrence rate of EPIs during the postsunset and postmidnight periods for four different longitudinal sectors: America-Atlantic (100–20°W) (Figures 5a and 5b), Africa (20°W to 60°E) (Figures 5c and 5d), Asia (60–140°E) (Figures 5e and 5f), and Pacific (140°E to 100°W) (Figures 5g and 5h). The bin size is half a month, and the distribution pattern has a clear seasonal preference: the postsunset EPIs are often observed during equinoxes, while the postmidnight EPIs mainly occur around solstices. From the spatial perspective, the longitudinal difference can be viewed more clearly. In the American-Atlantic sectors, the occurrence rate during the December solstice and equinoxes is reduced from postsunset (30–40%) to postmidnight (5–15%), while a considerable enhancement can be observed during the June solstice from postsunset (~5%) to postmidnight (15–20%). In the African sector, the situation is slightly different: The postsunset EPIs have a lower occurrence level (10–20%) and two minor peaks

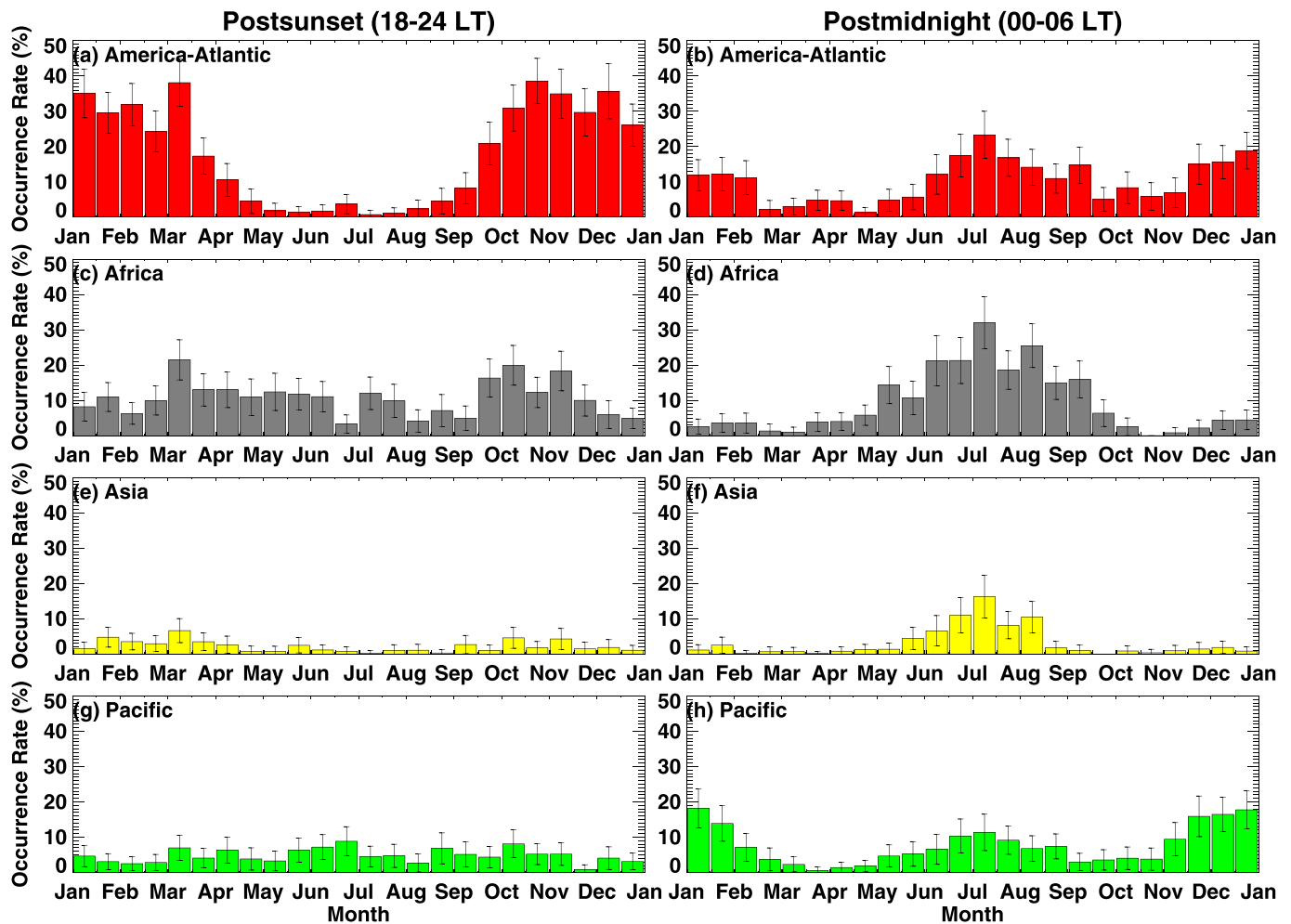


Figure 5. Monthly distribution of the EPI occurrence rate of equatorial plasma irregularities for four different longitudinal sectors during the postsunset and postmidnight periods, respectively. The bin size is half a month. The error bars are also marked. EPI = equatorial plasma irregularity.

near equinoxes. While the postmidnight EPIs have the most significant occurrence rate around the Northern Hemisphere summer solstice (20–35%) compared with the other longitudinal sectors. In the Asian and Pacific sectors, the general occurrence rate of postsunset EPIs is low, but the occurrence rate of the postmidnight EPIs exhibits a considerable enhancement during the June solstice for the Asian longitudes, and also during the December solstice at the Pacific longitudes.

3.2. local Time and Latitudinal Variation

Figure 6 shows the longitudinal-local time distribution of the occurrence rate of EPIs for different seasons with a resolution of 10° in longitude and 1 hr in local time. The occurrence rate is calculated as the ratio of the detected EPI numbers to the satellite crossing counts in each bin. Figure 7 further displays the occurrence rate variations as a function of local time at four different longitudinal sectors with error bars reflecting the uncertainty. In both Figures 6 and 7, it can be seen that EPI is basically a nighttime phenomenon with a significant occurrence rate peak around 20–21 LT during the December solstice and the equinoxes. The postsunset prereversal enhancement (PRE) of an eastward electric field is one of the most important generation mechanisms of plasma irregularities (Eccles et al., 2015), which can increase the equatorial upward drift velocity and provide a favorable condition for the R-T instability to develop. Thus, the occurrence rate of EPI usually reaches a peak after sunset. However, during the June solstice, the EPIs are more frequently observed in the postmidnight sector, especially over the African longitudes, with a maximum occurrence rate around 03–04 LT reaching 25–30%. This phenomenon is consistent with previous studies (e.g., Dao et al., 2011; Yizengaw et al., 2013), though the mechanisms for generating the postmidnight EPI peak are still unknown and widely debated. We will further discuss this topic in the discussion section.

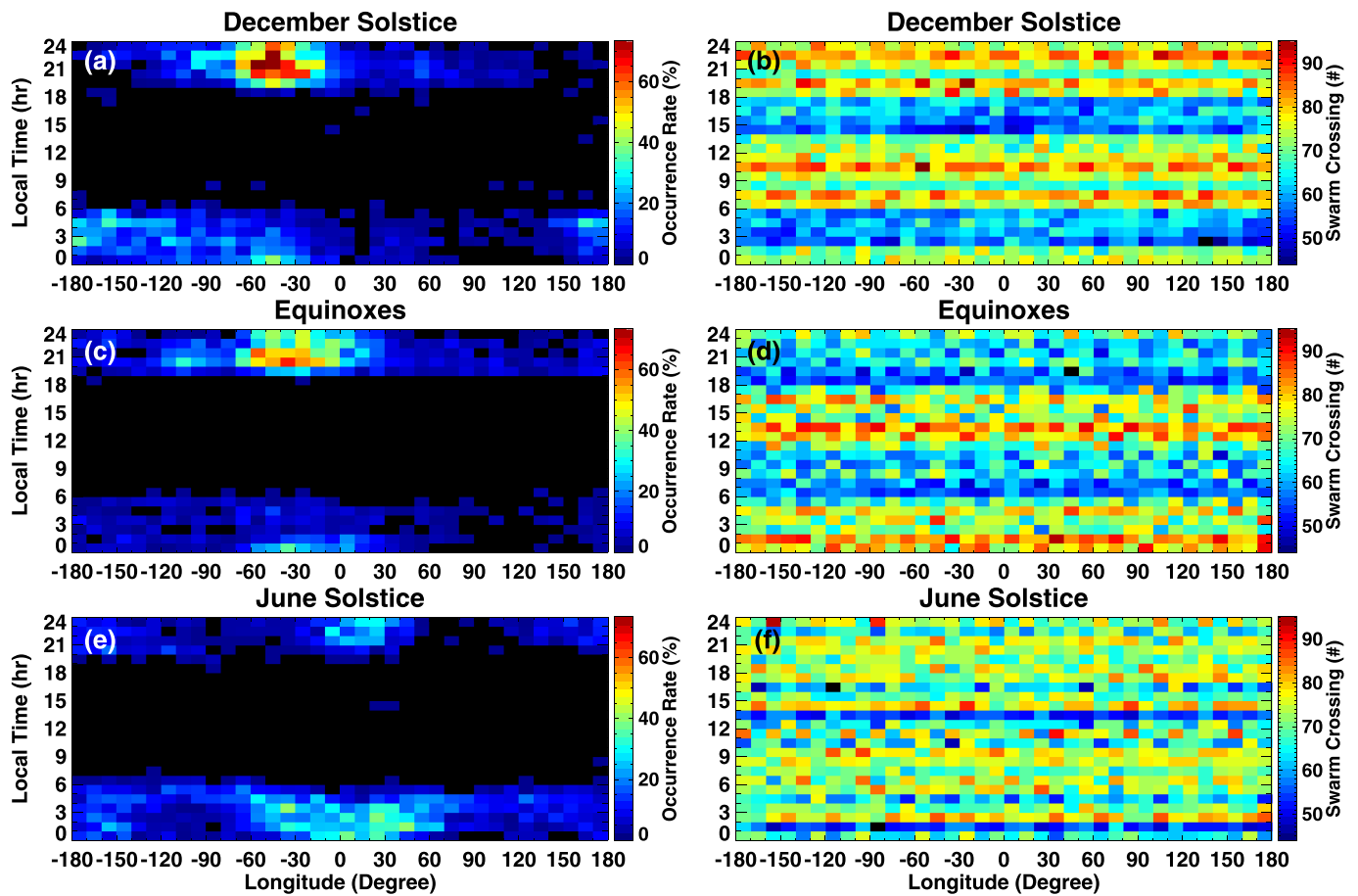


Figure 6. Longitudinal-local time distribution of the EPI occurrence rate (a, c, and e) and the Swarm crossing counts (b, d, and f) during the December solstice, equinoxes, and the June solstices. EPI = equatorial plasma irregularity.

In addition to the local time variations, it is also important to investigate the latitudinal dependence of the occurrence rate of EPIs. Considering the characteristics of EPIs are influenced by both the geomagnetic field configuration and the spinning of the Earth, we here adopted the coordinated system of magnetic latitude (MLAT) and magnetic local time (MLT) to do the analysis. Figures 8a–8c show the MLAT-MLT distribution of the occurrence rate of EPIs for different seasons with a resolution of 2° in magnetic latitude and 1 hr in magnetic local time. Moreover, the corresponding latitudinal variation for postsunset (Figures 8d–8f) and postmidnight (Figures 8g–8i) sectors are displayed. The latitudinal distribution exhibits a double-peak structure that can be fitted roughly by a bimodal distribution curve. The occurrence peaks are centered in two latitudinal bands north and south of the equator that is located approximately at $\pm 5^\circ$, which is similar with previous studies (Stolle et al., 2006; Xiong et al., 2010, 2012). One thing worth noting is that the northern peak is slightly higher than the southern peak during the June solstice and equinoxes in both local times, while the situation is reversed during the December solstice. It is known that the trans-equatorial wind may cause a decrease in the local conductivity on the upwind side (summer hemisphere) where the layer is raised and cause an increase in the local conductivity on the downwind side (winter hemisphere) where the layer is lowered. The latter effect is typically stronger than the former one due to the height-dependent ion composition, so there is a net increase in the total field-line integrated conductivity (Abdu, 2019; Huba & Krall, 2013; Maruyama, 1988). As a result, the nonlinear growth rate of the R-T instability will be suppressed in both hemispheres mainly due to the enhanced winter hemisphere conductivity. Moreover, in the winter hemisphere of high conductivity, polarization electric fields in the *F* region with smaller scales may be shorted out (Huang, 2016; Pudovkin, 1974), so that the instabilities for density irregularities near the bubble boundaries may be suppressed. This might contribute to the slightly lower occurrence rate of the irregularities in the winter hemisphere. More future work needs to be performed to further the understanding on this subtle asymmetry.

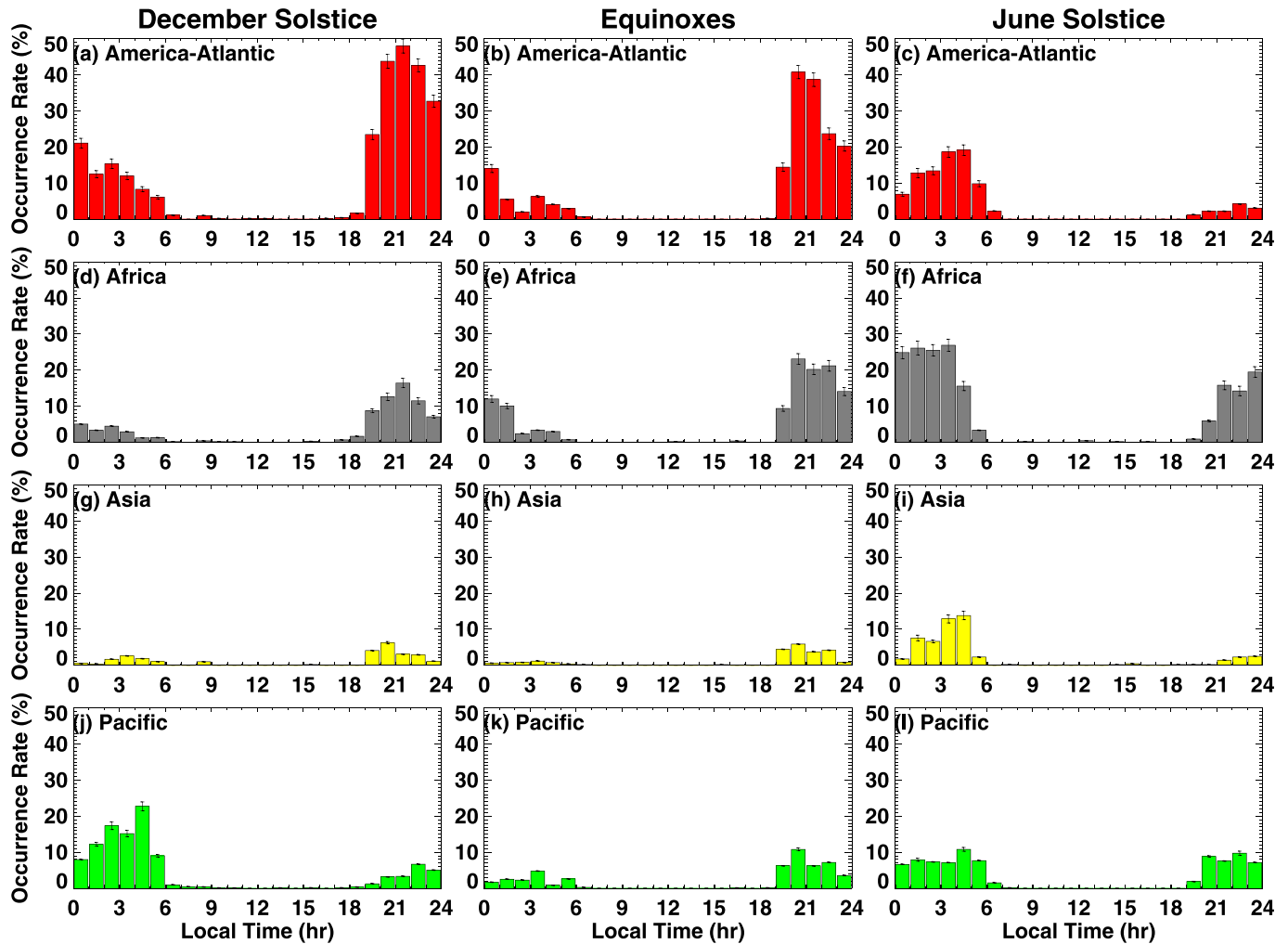


Figure 7. Local time variation of the EPI occurrence rate for four different longitudinal sectors during the December solstice (a, d, g, and j), equinoxes (b, e, h, and k), and the June solstice (c, f, i, and l). The error bars are also marked. EPI = equatorial plasma irregularity.

3.3. Dependence on Solar and Geomagnetic Activity

The Swarm measurements used in the current study start from December 2013, close to the solar maximum of Solar Cycle 24, and continue to the deep solar minimum in December 2019. In order to present solar-cycle and solar activity dependence of EPIs, Figures 9a and 9b show the multiyear longitudinal-monthly distribution of the EPI occurrence rate in the postsunset and postmidnight sectors with a resolution of 10° in longitude and 1 month. The middle panels show the Swarm data coverage for each longitudinal-monthly bin. It can be seen that the crossing counts exhibit specific systematic pattern with a period of around 4 months, which is due to that the Swarm satellites need ~ 120 days to get full coverage of 24-hr local time (Lühr et al., 2016). The seasonal and longitudinal variation of the occurrence rate is very similar with the global morphology shown in Figure 4: The postsunset EPIs have occurrence peak over the Atlantic-American sectors during the December solstice and equinoxes, while the postmidnight EPIs are most often observed in the African sector during the June solstice and in the Pacific sector during December solstice.

However, the solar activity dependence of the EPI occurrence rate in these two sectors exhibits opposite trends. As can be seen in Figures 9e and 9f, the postsunset EPIs have larger occurrence rate around solar maximum and gradually decrease with decreasing solar activity, but the occurrence rate of postmidnight EPIs exhibit a generally increasing trend with decreasing solar activity. Considering that the monthly data distribution is uneven due to the above-mentioned issue of local time coverage, this preliminary result of solar dependence needs to be further verified in a wider temporal window. Thus, Figures 10a and 10b show the

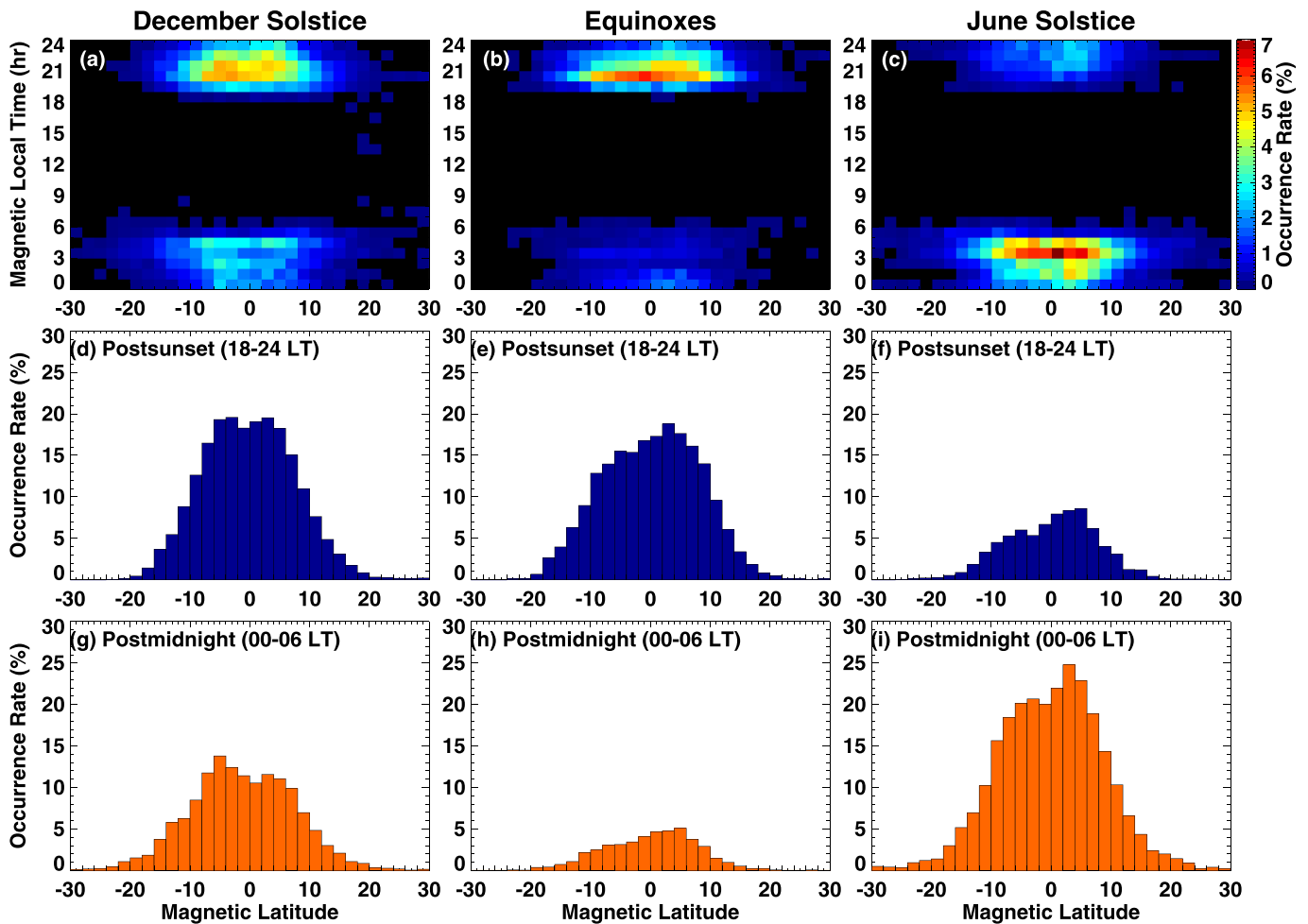


Figure 8. (a–c) Magnetic latitude and magnetic local time distribution of the EPI occurrence rate during the December solstice, equinoxes, and the June solstice, respectively. (d–i) Latitudinal variation of the EPI occurrence rate during the postsunset and postmidnight periods, respectively. EPI = equatorial plasma irregularity.

scatter plots of triannual (4-month) averaged F10.7 index versus EPI occurrence rate in the postsunset and postmidnight sectors, respectively. The postsunset EPIs and F10.7 index exhibit a positive correlation, with the coefficient equals to 0.83; the postmidnight comparison shows a negative correlation, and the coefficient equals to -0.74 . This opposite solar activity dependence will be further discussed in the next section.

To specify the geomagnetic activity dependence of the EPI occurrence rate, Figures 10c and 10d show the binned postsunset/postmidnight EPI occurrence rates as a function of the Kp value during both low solar activity ($F10.7 < 100$) and moderate to high solar activity ($F10.7 \geq 100$) levels, respectively. Both results show a similar developing trend. During the quiet geomagnetic time ($Kp = 0-3$), there is no consistent variation pattern for the occurrence rates. During active geomagnetic interval ($Kp > 3$), the occurrence rate exhibits slightly increasing trends with respect to the increasing Kp values, which might suggest that the conditions favorable to the growth of plasma irregularities are enhanced during high geomagnetic activity. However, the error bars are also increasing due to low data availability among high Kp intervals. This geomagnetic dependence is similar with those indicated in Stolle et al. (2006) and Huang et al. (2001). A comparison of low solar activity and high solar activity results also indicated that the postsunset and postmidnight EPI occurrence rate has opposite solar dependence.

4. Discussion

First of all, several studies have indicated that the smaller the angle between the equatorial magnetic field lines and the dusk terminator, the larger the EPI occurrence rate should be expected, because similar sunset

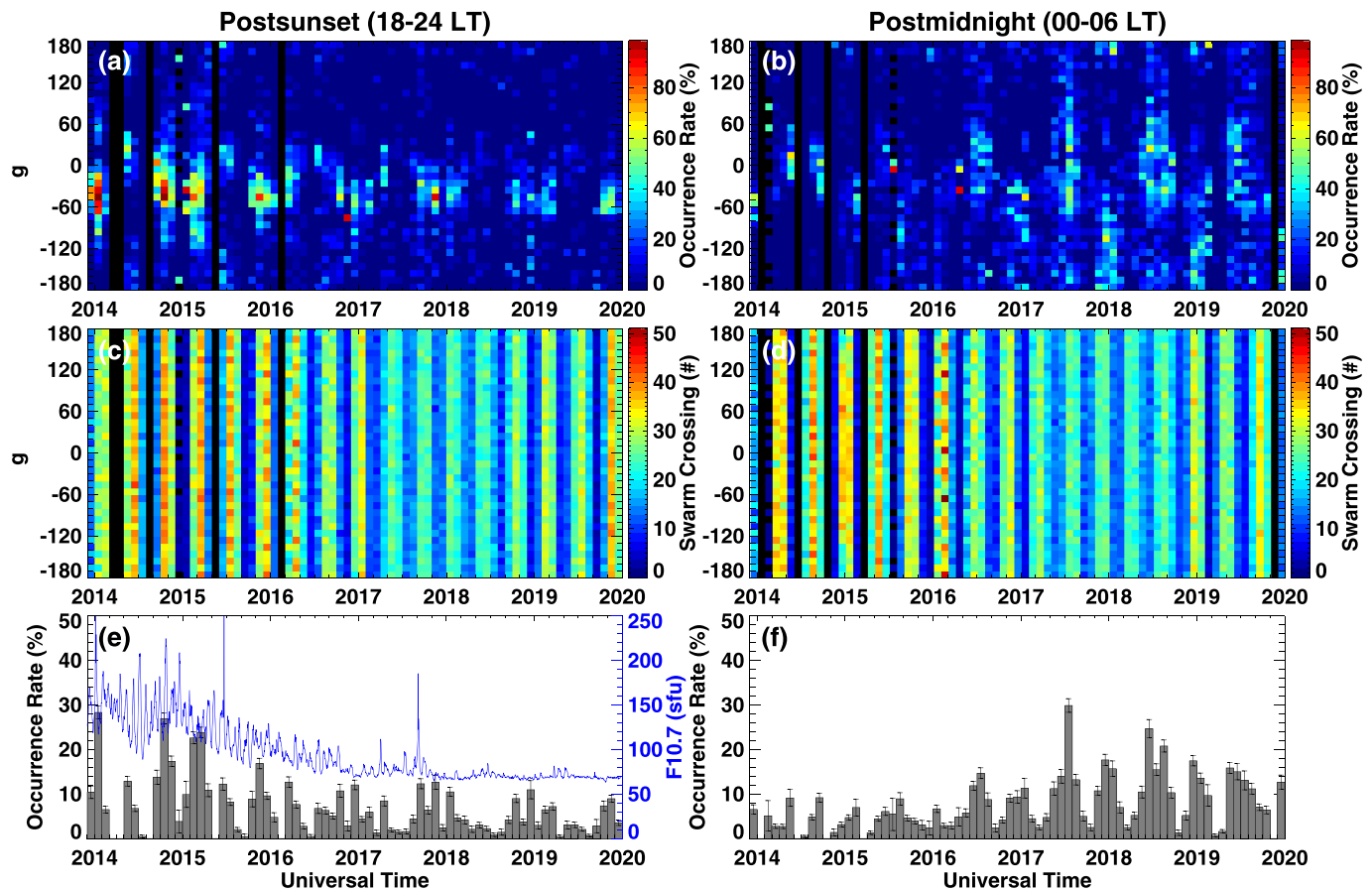


Figure 9. Multiyear longitudinal-monthly distribution of the EPI occurrence rate (top panels), the Swarm crossing counts (middle panels), and the monthly variation of the occurrence rate (bottom panels) during 2013–2019 for the postsunset and postmidnight periods. The temporal variation of daily F10.7 index is also plotted. EPI = equatorial plasma irregularity.

conditions can be met at the same time in the conjugate hemispheres and the flux tube-integrated conductance affecting the R-T instability growth rate is lower (e.g., Basu & Basu, 1985; Burke, Gentile, et al., 2004; Burke, Huang, et al., 2004; Otsuka, 2018; Tsunoda, 1985). At the South American and Atlantic longitudes, conditions for the minimum angle occur around February–March and October–November. This explains the more significant occurrence rates over these longitudinal sectors during the December solstice and equinoxes seasons as demonstrated in Figure 3. Moreover, the asymmetrical seasonal distribution seen during the December and the June solstice can also be explained by the interhemispheric winds that propagate from the summer hemisphere to the winter hemisphere (Burke, Gentile, et al., 2004; Burke, Huang, et al., 2004). The R-T instability growth rate will be suppressed by the interhemispheric winds as stated in the previous section, which can result in a higher occurrence rate of plasma irregularities over the longitudes where the magnetic equator is located in the summer hemisphere, that is, the African and Asian sectors in June–August and the East Pacific and American sector in December–February.

Second, there is a significant postsunset/postmidnight distribution asymmetry as shown in Figure 4: The postsunset EPIs are often observed over the Atlantic-American sectors during the December solstice and equinoxes, while the postmidnight EPIs have a large occurrence peak around the June solstice, especially in the African sector. Besides the above-mentioned declination angle and interhemispheric meridional wind effects, the longitudinal feature of postsunset EPI is also related to the equatorial vertical plasma drift that influenced by the geomagnetic field morphology. The South Atlantic Anomaly (SAA) area has the weakest geomagnetic field strength comparing with an idealized dipole field, and the Earth's inner radiation belt also dips down to the height of the ionospheric *F* region (Abdu et al., 2005). The R-T growth rate in the postsunset sector is strongly dependent on the vertical component of equatorial plasma drift that is expressed as $V_p = \mathbf{E} \times \mathbf{B}/B^2$, where \mathbf{E} is the zonal component of the electric field at the magnetic equator (Sultan, 1996).

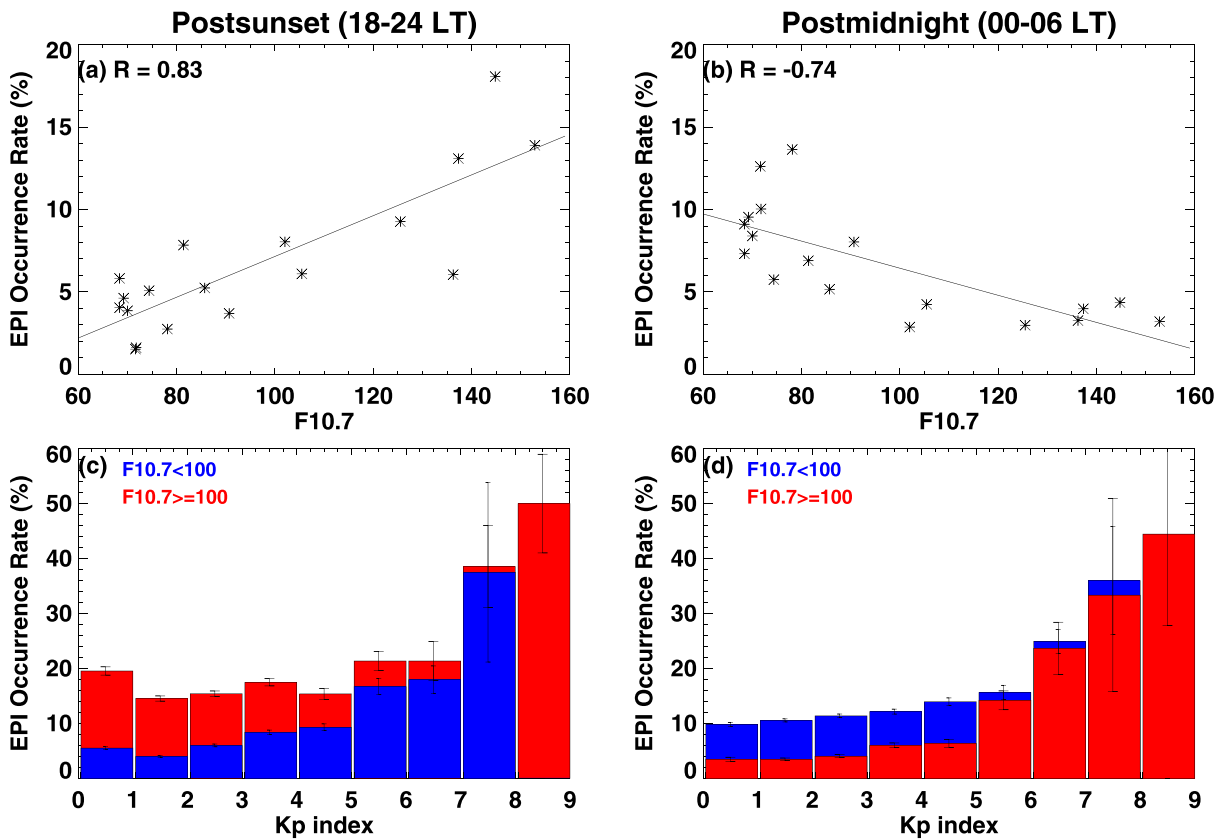


Figure 10. Scatter plots of the 4-month average F10.7 index versus the EPI occurrence rate during the (a) postsunset and (b) postmidnight periods; the EPI occurrence rate as a function of Kp index during the (c) postsunset and (d) postmidnight periods. The blue and red bars represent low solar activity ($F10.7 < 100$) and moderate to high solar activity ($F10.7 \geq 100$) situations, respectively. The bin of 0–1 includes the data with Kp equal to 0 and 1^- , and the bin of 1–2 include the data with Kp equal to 1^+ , 2^- , and so on. EPI = equatorial plasma irregularity.

Thus, assuming the postsunset zonal electric field is independent of longitude, the upward drift term in the growth rate calculation of R-T instability is favored in regions of low magnetic field intensity, especially in the area around the SAA (Burke, Gentile, et al., 2004; Burke, Huang, et al., 2004). Although the actual variation of the upward plasma drift is more complicated, many statistical studies have found that the observed climatological pattern of EPIs is closely correlated with the longitudinal and seasonal variations of V_p (e.g., Carter et al., 2013; Kil, Paxton, et al., 2009; Su et al., 2008; Yizengaw et al., 2014). Moreover, the eastward thermospheric wind, combined with shear flow, is another important factor in controlling the occurrence of postsunset EPIs. Kudeki et al. (2007) indicated that the vertical Pedersen currents induced by eastward wind are able to polarize the initial density perturbation into an unstable mode to trigger plasma bubbles. Liu et al. (2016) found that the thermospheric zonal wind is strongest around equinoxes and weakest around June solstice, which agrees perfectly to the seasonal patterns of postsunset EPIs. Thus, the longitudinal and seasonal distribution of postsunset EPIs is mainly controlled by equatorial vertical drift and thermospheric zonal wind.

The formation mechanisms of the postmidnight EPIs are still widely debated, which can be mainly attributed to either the continuation of EPIs generated in the premidnight hours (Bhattacharyya et al., 2001; Li et al., 2011), or irregularities freshly generated there owing to local plasma instabilities (Huang et al., 2010; Yizengaw et al., 2013). The above-mentioned seasonal and longitudinal anomaly of the postmidnight EPIs could be generated by more than one factors considering the growth rate of R-T instability depends on various external driving forces, such as neutral wind, electric and magnetic field, and background ionospheric features, such as flux-integrated Pedersen conductivity and upward density gradient (Abdu, 2001). Some studies found that the seasonal pattern of the F layer altitude exhibit a noticeable midnight uplift, especially around the June solstice due to the equatorward meridional neutral winds that are associated with midnight temperature maximum (e.g., Nicolls et al., 2006; Nishioka et al., 2012; Yokoyama et al., 2011). The

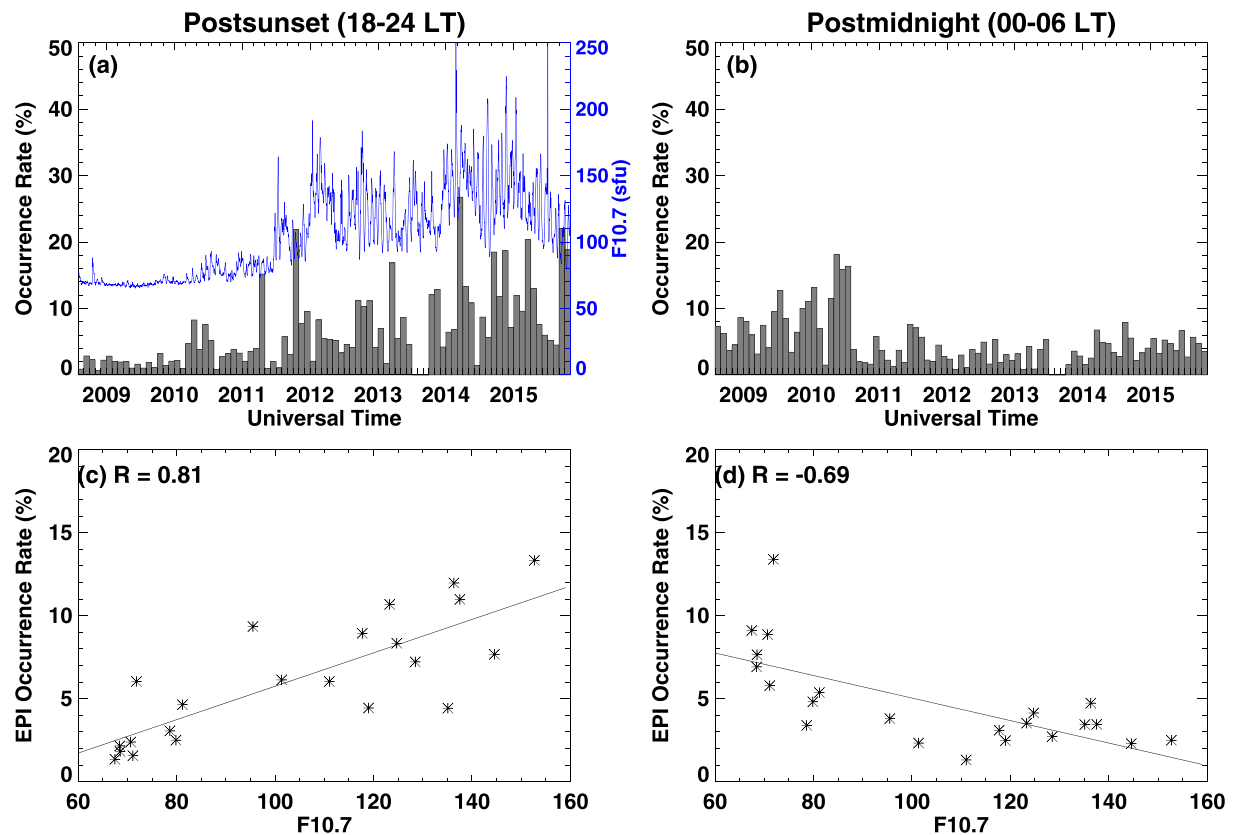


Figure 11. (a and b) Monthly variation of the postsunset/postmidnight EPI occurrence rate derived from C/NOFS in situ ion density during 2008–2015. The temporal variation of daily F10.7 index is also plotted. The gap in data during 2013 is the period when the satellite was placed into safe mode. (c and d) Scatter plots of the 4-month average F10.7 index versus the EPI occurrence rate. EPI = equatorial plasma irregularity. C/NOFS = Communications/Navigation Outage Forecasting System.

uplift of the *F* layer will cause a decrease in the ion-neutral collision frequency and thus increase the growth rate of the R-T instability. Furthermore, some other studies proposed that the localized gravity waves due to tropospheric convective activity near the intertropical convergence zone (ITCZ) could seed the bottomside irregularity to trigger the equatorial plasma bubbles, which might play a role in controlling the longitudinal dependence of EPIs since the convective process is more active over continental landmasses (especially for the African sector) than over the oceans (Yizengaw et al., 2013; Yizengaw & Groves, 2018). Recently, Liu et al. (2017) conducted a systematic survey of medium-scale atmospheric gravity waves. They found that there are stronger perturbations over continents than over oceans and the gravity wave activities maximize around June solstice and minimize around equinoxes. These gravity wave features highly resemble those of postmidnight EPIs indicated in our study. These points could possibly explain why the postmidnight EPIs are more often observed during the June solstice and over the African sector, though more extensive evidence is still needed.

Last but not least, the role of solar and geomagnetic activities in the EPI occurrence rate needs to be further specified. Many previous studies have seemingly conflicting results of the solar activity dependence as we described in section 1. In the current study, opposite solar activity dependencies were discovered for the postsunset and postmidnight EPIs. In order to further validate this opposite solar cycle dependence, we here also used the in situ ion density data from the Ion Velocity Meter onboard the Communications/Navigation Outage Forecasting System (C/NOFS) from August 2008 to November 2015 to conduct a similar solar dependence study. C/NOFS has a low Earth orbit with a 13° inclination, a perigee near 400 km, and an apogee near 850 km. The same algorithm specified in section 2 is applied to C/NOFS in situ ion density with a time cadence of 1 Hz. Figure 11 shows the solar cycle dependence of EPIs by using C/NOFS data, which has the same feature with those of Swarm result that the postsunset EPI is positively correlated with the F10.7 index and the postmidnight EPI is negatively correlated with F10.7 index. So the contradictory results could be

depending on whether the majority of the EPI events in their database is in the postsunset or postmidnight sector. However, a new question is also raised: Why the postmidnight EPIs exhibit a different solar activity dependence pattern? Otsuka (2018) analyzed the g/v_{in} term in the linear growth rate of the R-T instability, where g is the gravity acceleration and v_{in} is the ion-neutral collision frequency. This term is larger during the nighttime than the daytime and increases with decreasing solar activity since the collision frequency v_{in} is proportional to the neutral density, which is lower during the nighttime and also during solar minimum. Furthermore, Liu et al. (2017) indicated that gravity wave activities are stronger at low solar flux levels, which agrees well with that of postmidnight EPIs. These points could possibly explain the anticorrelation between the postmidnight EPIs and F10.7, though a more quantitative calculation is still needed to confirm whether these effects are significant enough. As for the geomagnetic activity dependence, the occurrence rate is collectively influenced by the existence and interaction of prompt penetration electric field, disturbance wind dynamo electric field, and shielding electric field. EPIs can be enhanced or suppressed for individual storm cases over different local time sectors, but a net effect shown by Figure 10d is that the occurrence rates are enhanced during high geomagnetic activity period, although the error bars are considerably increased for higher Kp intervals. The geomagnetic activity can impact the EPIs immediately in the case of penetrating electric fields or with a specific time delay in the case of disturbance dynamo. Typically, the largest Kp occurs during the main phase of a storm, and the disturbance dynamo has not fully developed yet, so EPIs tend to have a higher occurrence rate. During moderate Kp, such as 4–6, this is usually a mixture of main and recovery phases, so the electrodynamics are not very clear. Thus, the role of geomagnetic activity in influencing EPIs occurrence rate distribution is still an open question and needs to use numerical models to make a further study in the future.

5. Conclusion

In this paper, we present a statistical study of the EPI occurrence rates in the ionospheric F layer by using 6 years in situ plasma density measurements from the Swarm constellation. The occurrence patterns in terms of longitude, season, local time, latitude, solar activity, and geomagnetic activity levels are analyzed. The major controlling factors of the spatial-temporal distribution of the postsunset and postmidnight EPIs are also discussed. The main findings and results are summarized as follows:

1. The statistical results from the Swarm and C/NOFS collectively support the feature that postsunset and postmidnight EPI occurrence rates have opposite dependencies on solar activity. The former is positively correlated with the F10.7 index, while the latter is negatively correlated with it.
2. The postsunset and postmidnight EPIs have asymmetric occurrence distribution. The postsunset EPIs have more significant occurrence rates during the December solstice and equinoxes with a clear longitudinal preference for the Atlantic-American sector. On the other hand, the postmidnight EPIs are more prominent than the postsunset ones during the June solstice with the strongest occurrence peak occurring over the African sector, while the Pacific sector exhibits a considerable postmidnight occurrence enhancement during the December solstice. The occurrence rate around equinoxes within this local time sector is substantially reduced. The main controlling factors for the distribution of postsunset EPIs are the magnetic declination effect, equatorial vertical $E \times B$ drift, and thermospheric zonal wind. For the postmidnight EPIs, the main controlling factors are likely to be atmospheric gravity waves and equatorward thermospheric wind associated with midnight temperature maximum.
3. The latitudinal distribution of EPIs exhibits a double-peak structure, with the maximum occurrence rates located around $\pm 5^\circ$ magnetic latitude. The Northern Hemisphere peak is slightly higher than the Southern Hemisphere peak during the June solstice and equinoxes, while the situation is reversed during the December solstice. This hemispheric asymmetry might be attributed to the effects of trans-equatorial thermospheric wind.
4. Most of the EPIs are constrained within 30° away from the magnetic equator, and their spatial distribution has a noticeable longitudinal preference. The density irregularity is more frequently detected over the South American sector in the December solstice with the occurrence rate ranging from 40–80%. The longitudinal preference of EPIs extends to the Atlantic and African sectors in the March/September equinoxes, while the occurrence rate over these regions reduces to 20–50%. As for the June solstice, the distribution is relatively even with broader longitude coverage, and the peak of occurrence rate shifts to the African sector.

5. The local time distribution of EPIs also exhibits asymmetric patterns over different season/longitudes. During the December solstice and equinoxes, the occurrence rate has peak value in the evening sector around 20–21 LT and becomes much lower after midnight except for the Pacific sector. During the June solstice, the EPI occurrence rate often slowly increases after sunset and reaches a peak value after midnight around 03–04 LT.
6. The general level of EPI occurrence rate increases with respect to the increasing geomagnetic activity level, although the corresponding error bars also increase.

Acknowledgments

This work is sponsored by the Strategic Priority Research Program of Chinese Academy of Sciences (XDA17010302), National Key R&D Program of China (2016YFB0501503), National Science Foundation of China (41674183 and 41974184), Youth Innovation Promotion Association of Chinese Academy of Sciences, and Shenzhen Technology Project JJC20160817172025986. We greatly acknowledge ESA for SWARM data (<http://earth.esa.int/swarm>). The F10.7 data are acquired from NASA/GSFC's Space Physics Data Facility's OMNIWeb service (<https://cdaweb.gsfc.nasa.gov/>). Kp indices are downloaded from Kyoto world data center for Geomagnetism (<http://wdc.kugi.kyoto-u.ac.jp/>). The C/NOFS in situ ion density data is available from NASA/GSFC's Space Physics Data Facility's OMNIWeb service (<https://cdaweb.sci.gsfc.nasa.gov/>).

References

- Aa, E., Huang, W., Liu, S., Ridley, A., Zou, S., Shi, L., et al. (2018). Midlatitude plasma bubbles over China and adjacent areas during a magnetic storm on 8 September 2017. *Space Weather*, *16*, 321–331. <https://doi.org/10.1002/2017SW001776>
- Aa, E., Zou, S., Eastes, R., Karan, D. K., Zhang, S.-R., Erickson, P. J., & Coster, A. J. (2020). Coordinated ground-based and space-based observations of equatorial plasma bubbles. *Journal of Geophysical Research: Space Physics*, *125*, e2019JA027569. <https://doi.org/10.1029/2019JA027569>
- Aa, E., Zou, S., Ridley, A. J., Zhang, S.-R., Coster, A. J., Erickson, P. J., et al. (2019). Merging of storm-time midlatitude traveling ionospheric disturbances and equatorial plasma bubbles. *Space Weather*, *17*, 285–298. <https://doi.org/10.1029/2018SW002101>
- Abdu, M. A. (2001). Outstanding problems in the equatorial ionosphere-thermosphere electrodynamics relevant to spread F. *Journal of Atmospheric and Solar-Terrestrial Physics*, *63*(9), 869–884. [https://doi.org/10.1016/S1364-6826\(00\)00201-7](https://doi.org/10.1016/S1364-6826(00)00201-7)
- Abdu, M. A. (2019). Day-to-day and short-term variabilities in the equatorial plasma bubble/spread F irregularity seeding and development. *Progress in Earth and Planetary Science*, *6*, 11. <https://doi.org/10.1186/s40645-019-0258-1>
- Abdu, M. A., Batista, I. S., Carrasco, A. J., & Brum, C. G. (2005). South Atlantic magnetic anomaly ionization: A review and a new focus on electrodynamic effects in the equatorial ionosphere. *Journal of Atmospheric and Solar-Terrestrial Physics*, *67*(17), 1643–1657. <https://doi.org/10.1016/j.jastp.2005.01.014>
- Abdu, M. A., Batista, I. S., Takahashi, H., MacDougall, J., Sobral, J. H., Medeiros, A. F., & Trivedi, N. B. (2003). Magnetospheric disturbance induced equatorial plasma bubble development and dynamics: A case study in Brazilian sector. *Journal of Geophysical Research*, *108*(A12), 1449. <https://doi.org/10.1029/2002JA009721>
- Aveiro, H. C., Hysell, D. L., Caton, R. G., Groves, K. M., Klenzing, J., Pfaff, R. F., et al. (2012). Three-dimensional numerical simulations of equatorial spread F: Results and observations in the Pacific sector. *Journal of Geophysical Research*, *117*, A03325. <https://doi.org/10.1029/2011JA017077>
- Basu, S., & Basu, S. (1985). Equatorial scintillations: Advances since ISEA-6. *Journal of Atmospheric and Terrestrial Physics*, *47*(8), 753–768. [https://doi.org/10.1016/0021-9169\(85\)90052-2](https://doi.org/10.1016/0021-9169(85)90052-2)
- Basu, S., Basu, S., Groves, K. M., Yeh, H.-C., Su, S.-Y., Rich, F. J., et al. (2001). Response of the equatorial ionosphere in the South Atlantic Region to the Great Magnetic Storm of July 15, 2000. *Geophysical Research Letters*, *28*, 3577–3580. <https://doi.org/10.1029/2001GL013259>
- Bhattacharyya, A., Basu, S., Groves, K. M., Valladares, C. E., & Sheehan, R. (2001). Dynamics of equatorial F region irregularities from spaced receiver scintillation observations. *Geophysical Research Letters*, *28*, 119–122. <https://doi.org/10.1029/2000GL01228>
- Blanch, E., Altadill, D., Juan, J. M., Camps, A., Barbosa, J., González-Casado, G., et al. (2018). Improved characterization and modeling of equatorial plasma depletions. *Journal of Space Weather and Space Climate*, *8*, A38. <https://doi.org/10.1051/swsc/2018026>
- Burke, W. J., Gentile, L. C., Huang, C. Y., Valladares, C. E., & Su, S. Y. (2004). Longitudinal variability of equatorial plasma bubbles observed by DMSP and ROCSAT-1. *Journal of Geophysical Research*, *109*, A12301. <https://doi.org/10.1029/2004JA010583>
- Burke, W., Huang, C., Gentile, L., & Bauer, L. (2004). Seasonal-longitudinal variability of equatorial plasma bubbles. *Annales Geophysicae*, *22*, 3089–3098. <https://doi.org/10.5194/angeo-22-3089-2004>
- Carter, B. A., Yizengaw, E., Pradipta, R., Retterer, J. M., Groves, K., Valladares, C., et al. (2016). Global equatorial plasma bubble occurrence during the 2015 St. Patrick's Day storm. *Journal of Geophysical Research: Space Physics*, *121*, 894–905. <https://doi.org/10.1002/2015JA022194>
- Carter, B. A., Zhang, K., Norman, R., Kumar, V. V., & Kumar, S. (2013). On the occurrence of equatorial F-region irregularities during solar minimum using radio occultation measurements. *Journal of Geophysical Research: Space Physics*, *118*, 892–904. <https://doi.org/10.1002/jgra.50089>
- Cherniak, I., & Zakharenkova, I. (2016). First observations of super plasma bubbles in Europe. *Geophysical Research Letters*, *43*, 11,137–11,145. <https://doi.org/10.1002/2016GL071421>
- Cherniak, I., Zakharenkova, I., & Sokolovsky, S. (2019). Multi-instrumental observation of storm-induced ionospheric plasma bubbles at equatorial and middle latitudes. *Journal of Geophysical Research: Space Physics*, *124*, 1491–1508. <https://doi.org/10.1029/2018JA026309>
- Comberiate, J., & Paxton, L. J. (2010). Coordinated UV imaging of equatorial plasma bubbles using TIMED/GUVI and DMSP/SSUSI. *Space Weather*, *8*, S10002. <https://doi.org/10.1029/2009SW000546>
- Dao, E., Kelley, M. C., Roddy, P., Retterer, J., Ballenthin, J. O., de La Beaujardiere, O., & Su, Y.-J. (2011). Longitudinal and seasonal dependence of nighttime equatorial plasma density irregularities during solar minimum detected on the C/NOFS satellite. *Geophysical Research Letters*, *38*, L10104. <https://doi.org/10.1029/2011GL047046>
- Eccles, J. V., St. Maurice, J. P., & Schunk, R. W. (2015). Mechanisms underlying the prereversal enhancement of the vertical plasma drift in the low-latitude ionosphere. *Journal of Geophysical Research: Space Physics*, *120*, 4950–4970. <https://doi.org/10.1002/2014JA020664>
- Fejer, B. G., Scherliess, L., & de Paula, E. R. (1999). Effects of the vertical plasma drift velocity on the generation and evolution of equatorial spread F. *Journal of Geophysical Research*, *104*, 19,859–19,870. <https://doi.org/10.1029/1999JA900271>
- Gentile, L. C., Burke, W. J., & Rich, F. J. (2006). A global climatology for equatorial plasma bubbles in the topside ionosphere. *Annales Geophysicae*, *24*(1), 163–172. <https://doi.org/10.5194/angeo-24-163-2006>
- Huang, C.-S. (2016). Plasma drifts and polarization electric fields associated with TID-like disturbances in the low-latitude ionosphere: C/NOFS observations. *Journal of Geophysical Research: Space Physics*, *121*, 1802–1812. <https://doi.org/10.1002/2015JA022201>
- Huang, C. Y., Burke, W. J., Machuzak, J. S., Gentile, L. C., & Sultan, P. J. (2001). DMSP observations of equatorial plasma bubbles in the topside ionosphere near solar maximum. *Journal of Geophysical Research*, *106*, 8131–8142. <https://doi.org/10.1029/2000JA000319>
- Huang, C. Y., Burke, W. J., Machuzak, J. S., Gentile, L. C., & Sultan, P. J. (2002). Equatorial plasma bubbles observed by DMSP satellites during a full solar cycle: Toward a global climatology. *Journal of Geophysical Research*, *107*(A12), 1434. <https://doi.org/10.1029/2002JA009452>

- Huang, C.-S., de La Beaujardiere, O., Roddy, P. A., Hunton, D. E., Ballenthin, J. O., & Hairston, M. R. (2012). Generation and characteristics of equatorial plasma bubbles detected by the C/NOFS satellite near the sunset terminator. *Journal of Geophysical Research*, *117*, A11313. <https://doi.org/10.1029/2012JA018163>
- Huang, C.-S., Foster, J. C., & Sahai, Y. (2007). Significant depletions of the ionospheric plasma density at middle latitudes: A possible signature of equatorial spread F bubbles near the plasmopause. *Journal of Geophysical Research*, *112*, A05315. <https://doi.org/10.1029/2007JA012307>
- Huang, C.-S., La Beaujardiere, O., Roddy, P. A., Hunton, D. E., Liu, J. Y., & Chen, S. P. (2014). Occurrence probability and amplitude of equatorial ionospheric irregularities associated with plasma bubbles during low and moderate solar activities (2008–2012). *Journal of Geophysical Research: Space Physics*, *119*, 1186–1199. <https://doi.org/10.1002/2013JA019212>
- Huang, C.-S., Rich, F. J., & Burke, W. J. (2010). Storm time electric fields in the equatorial ionosphere observed near the dusk meridian. *Journal of Geophysical Research*, *115*, A08313. <https://doi.org/10.1029/2009JA015150>
- Huba, J. D., & Joyce, G. (2007). Equatorial spread F modeling: Multiple bifurcated structures, secondary instabilities, large density 'bite-outs,' and supersonic flows. *Geophysical Research Letters*, *34*, L07105. <https://doi.org/10.1029/2006GL028519>
- Huba, J. D., Joyce, G., & Krall, J. (2008). Three-dimensional equatorial spread F modeling. *Geophysical Research Letters*, *35*, L10102. <https://doi.org/10.1029/2008GL033509>
- Huba, J. D., & Krall, J. (2013). Impact of meridional winds on equatorial spread F: Revisited. *Geophysical Research Letters*, *40*, 1268–1272. <https://doi.org/10.1002/grl.50292>
- Jin, H., Zou, S., Chen, G., Yan, C., Zhang, S., & Yang, G. (2018). Formation and evolution of low-latitude F region field-aligned irregularities during the 7–8 September 2017 storm: Hainan Coherent Scatter Phased Array Radar and Digisonde Observations. *Space Weather*, *16*, 648–659. <https://doi.org/10.1029/2018SW001865>
- Katamzi-Joseph, Z. T., Habarulema, J. B., & Hernández-Pajares, M. (2017). Midlatitude postsunset plasma bubbles observed over Europe during intense storms in April 2000 and 2001. *Space Weather*, *15*, 1177–1190. <https://doi.org/10.1002/2017SW001674>
- Kelley, M. C., Haerendel, G., Kappler, H., Valenzuela, A., Balsley, B. B., Carter, D. A., et al. (1976). Evidence for a Rayleigh-Taylor type instability and upwelling of depleted density regions during equatorial spread F. *Geophysical Research Letters*, *3*, 448–450. <https://doi.org/10.1029/GL003i008p00448>
- Kelley, M. C., Makela, J. J., Paxton, L. J., Kamalabadi, F., Comberiate, J. M., & Kil, H. (2003). The first coordinated ground- and space-based optical observations of equatorial plasma bubbles. *Geophysical Research Letters*, *30*(14), 1766. <https://doi.org/10.1029/2003GL017301>
- Kil, H., & Heelis, R. A. (1998). Global distribution of density irregularities in the equatorial ionosphere. *Journal of Geophysical Research*, *103*, 407–418. <https://doi.org/10.1029/97JA02698>
- Kil, H., Heelis, R. A., Paxton, L. J., & Oh, S.-J. (2009). Formation of a plasma depletion shell in the equatorial ionosphere. *Journal of Geophysical Research*, *114*, A11302. <https://doi.org/10.1029/2009JA014369>
- Kil, H., Paxton, L. J., & Oh, S.-J. (2009). Global bubble distribution seen from ROCSAT-1 and its association with the evening prereversal enhancement. *Journal of Geophysical Research*, *114*, A06307. <https://doi.org/10.1029/2008JA013672>
- Krall, J., Huba, J. D., Ossakow, S. L., Joyce, G., Makela, J. J., Miller, E. S., & Kelley, M. C. (2011). Modeling of equatorial plasma bubbles triggered by non-equatorial traveling ionospheric disturbances. *Geophysical Research Letters*, *38*, L08103. <https://doi.org/10.1029/2011GL046890>
- Kudeki, E., Akgiray, A., Milla, M., Chau, J. L., & Hysell, D. L. (2007). Equatorial spread-F initiation: Post-sunset vortex, thermospheric winds, gravity waves. *Journal of Atmospheric and Solar-Terrestrial Physics*, *69*(17–18), 2416–2427. <https://doi.org/10.1016/j.jastp.2007.04.012>
- Lühr, H., Kervalishvili, G., Rauberg, J., & Stolle, C. (2016). Zonal currents in the F region deduced from Swarm constellation measurements. *Journal of Geophysical Research: Space Physics*, *121*, 638–648. <https://doi.org/10.1002/2015JA022051>
- Lühr, H., Xiong, C., Park, J., & Rauberg, J. (2014). Systematic study of intermediate-scale structures of equatorial plasma irregularities in the ionosphere based on CHAMP observations. *Frontiers in Physics*, *2*, 15. <https://doi.org/10.3389/fphy.2014.00015>
- Li, G., Ning, B., Abdu, M. A., Otsuka, Y., Yokoyama, T., Yamamoto, M., & Liu, L. (2013). Longitudinal characteristics of spread F backscatter plumes observed with the EAR and Sanya VHF radar in Southeast Asia. *Journal of Geophysical Research: Space Physics*, *118*, 6544–6557. <https://doi.org/10.1002/jgra.50581>
- Li, G., Ning, B., Abdu, M. A., Yue, X., Liu, L., Wan, W., & Hu, L. (2011). On the occurrence of postmidnight equatorial F region irregularities during the June solstice. *Journal of Geophysical Research*, *116*, A04318. <https://doi.org/10.1029/2010JA016056>
- Li, G., Ning, B., Wang, C., Abdu, M. A., Otsuka, Y., Yamamoto, M., et al. (2018). Storm-enhanced development of post-sunset equatorial plasma bubbles around the meridian 120E/60W on 7–8 September 2017. *Journal of Geophysical Research: Space Physics*, *123*, 7985–7998. <https://doi.org/10.1029/2018JA025871>
- Liu, H., Doornbos, E., & Nakashima, J. (2016). Thermospheric wind observed by GOCE: Wind jets and seasonal variations. *Journal of Geophysical Research: Space Physics*, *121*, 6901–6913. <https://doi.org/10.1002/2016JA022938>
- Liu, H., Pedatella, N., & Hocke, K. (2017). Medium-scale gravity wave activity in the bottomside F region in tropical regions. *Geophysical Research Letters*, *44*, 7099–7105. <https://doi.org/10.1002/2017GL073855>
- Ma, G., & Maruyama, T. (2006). A super bubble detected by dense GPS network at east Asian longitudes. *Geophysical Research Letters*, *33*, L21103. <https://doi.org/10.1029/2006GL027512>
- Makela, J. J., & Kelley, M. C. (2003). Field-aligned 777.4-nm composite airglow images of equatorial plasma depletions. *Geophysical Research Letters*, *30*(8), 1442. <https://doi.org/10.1029/2003GL017106>
- Makela, J. J., & Miller, E. S. (2011). Influences on the development of equatorial plasma bubbles: Insights from a long-term optical dataset. In *Aeronomy of the Earth's Atmosphere and Ionosphere* (pp. 239–249). Dordrecht: Springer Netherlands.
- Martinis, C., Baumgardner, J., Mendillo, M., Wroten, J., Coster, A., & Paxton, L. (2015). The night when the auroral and equatorial ionospheres converged. *Journal of Geophysical Research: Space Physics*, *120*, 8085–8095. <https://doi.org/10.1002/2015JA021555>
- Maruyama, T. (1988). A diagnostic model for equatorial spread F. 1. Model description and application to electric field and neutral wind effects. *Journal of Geophysical Research*, *93*(A12), 14,611–14,622.
- Nicolls, M. J., Kelley, M. C., Vlasov, M. N., Sahai, Y., Chau, J. L., Hysell, D. L., et al. (2006). Observations and modeling of post-midnight uplifts near the magnetic equator. *Annales Geophysicae*, *24*, 1317–1331. <https://doi.org/10.5194/angeo-24-1317-2006>
- Nishioka, M., Otsuka, Y., Shiokawa, K., Tsugawa, T., Effendy, N., Supnithi, P., et al. (2012). On post-midnight field-aligned irregularities observed with a 30.8-MHz radar at a low latitude: Comparison with F-layer altitude near the geomagnetic equator. *Journal of Geophysical Research*, *117*, A08337. <https://doi.org/10.1029/2012JA017692>
- Nishioka, M., Saito, A., & Tsugawa, T. (2008). Occurrence characteristics of plasma bubble derived from global ground-based GPS receiver networks. *Journal of Geophysical Research*, *113*, A05301. <https://doi.org/10.1029/2007JA012605>

- Otsuka, Y. (2018). Review of the generation mechanisms of post-midnight irregularities in the equatorial and low-latitude ionosphere. *Progress in Earth and Planetary Science*, 5, 57. <https://doi.org/10.1186/s40645-018-0212-7>
- Ott, E. (1978). Theory of Rayleigh-Taylor bubbles in the equatorial ionosphere. *Journal of Geophysical Research*, 83, 2066–2070. <https://doi.org/10.1029/JA083iA05p02066>
- Pudovkin, M. I. (1974). Electric fields and currents in the ionosphere. *Space Science Reviews*, 16(5-6), 727–770. <https://doi.org/10.1007/BF00182599>
- Retterer, J. M., & Gentile, L. C. (2009). Modeling the climatology of equatorial plasma bubbles observed by DMSP. *Radio Science*, 44, RS0A31. <https://doi.org/10.1029/2008RS004057>
- Retterer, J. M., & Roddy, P. (2014). Faith in a seed: on the origins of equatorial plasma bubbles. *Annal Geophysicae*, 32, 485–498. <https://doi.org/10.5194/angeo-32-485-2014>
- Rodríguez-Zuluaga, J., Stolle, C., & Park, J. (2017). On the direction of the Poynting flux associated with equatorial plasma depletions as derived from Swarm. *Geophysical Research Letters*, 44, 5884–5891. <https://doi.org/10.1002/2017GL073385>
- Smith, J., & Heelis, R. A. (2017). Equatorial plasma bubbles: Variations of occurrence and spatial scale in local time, longitude, season, and solar activity. *Journal of Geophysical Research: Space Physics*, 122, 5743–5755. <https://doi.org/10.1002/2017JA024128>
- Stolle, C., Lühr, H., Rother, M., & Balasis, G. (2006). Magnetic signatures of equatorial spread F as observed by the CHAMP satellite. *Journal of Geophysical Research*, 111, A02304. <https://doi.org/10.1029/2005JA011184>
- Su, S.-Y., Chao, C. K., & Liu, C. H. (2008). On monthly/seasonal/longitudinal variations of equatorial irregularity occurrences and their relationship with the postsunset vertical drift velocities. *Journal of Geophysical Research*, 113, A05307. <https://doi.org/10.1029/2007JA012809>
- Su, S.-Y., Liu, C. H., Ho, H. H., & Chao, C. K. (2006). Distribution characteristics of topside ionospheric density irregularities: Equatorial versus midlatitude regions. *Journal of Geophysical Research*, 111, A06305. <https://doi.org/10.1029/2005JA011330>
- Sultan, P. J. (1996). Linear theory and modeling of the Rayleigh-Taylor instability leading to the occurrence of equatorial spread F. *Journal of Geophysical Research*, 101, 26,875–26,892. <https://doi.org/10.1029/96JA00682>
- Tsunoda, R. T. (1980). Magnetic-field-aligned characteristics of plasma bubbles in the nighttime equatorial ionosphere. *Journal Atmospheric Terrestrial Physical*, 42, 743–752. <https://doi.org/10.1002/2017JA024128>
- Tsunoda, R. T. (1985). Control of the seasonal and longitudinal occurrence of equatorial scintillations by the longitudinal gradient in integrated E region Pedersen conductivity. *Journal of Geophysical Research*, 90, 447–456. <https://doi.org/10.1029/JA090iA01p00447>
- Tsunoda, R. T., Livingston, R. C., McClure, J. P., & Hanson, W. B. (1982). Equatorial plasma bubbles—Vertically elongated wedges from the bottomside F layer. *Journal of Geophysical Research*, 87, 9171–9180. <https://doi.org/10.1029/JA087iA11p09171>
- Wan, X., Xiong, C., Rodríguez-Zuluaga, J., Kervalishvili, G. N., Stolle, C., & Wang, H. (2018). Climatology of the occurrence rate and amplitudes of local time distinguished equatorial plasma depletions observed by Swarm satellite. *Journal of Geophysical Research: Space Physics*, 123, 3014–3026. <https://doi.org/10.1002/2017JA025072>
- Woodman, R. F., & La Hoz, C. (1976). Radar observations of F region equatorial irregularities. *Journal of Geophysical Research*, 81(31), 5447–5466. <https://doi.org/10.1029/JA081i031p05447>
- Xiong, C., Lühr, H., Ma, S. Y., Stolle, C., & Fejer, B. G. (2012). Features of highly structured equatorial plasma irregularities deduced from CHAMP observations. *Annales Geophysicae*, 30, 1259–1269. <https://doi.org/10.5194/angeo-30-1259-2012>
- Xiong, C., Park, J., Lühr, H., Stolle, C., & Ma, S. Y. (2010). Comparing plasma bubble occurrence rates at CHAMP and GRACE altitudes during high and low solar activity. *Annales Geophysicae*, 28, 1647–1658. <https://doi.org/10.5194/698angeo-28-1647-2010>
- Xiong, C., Stolle, C., Lühr, H., Park, J., Fejer, B. G., & Kervalishvili, G. N. (2016). Scale analysis of equatorial plasma irregularities derived from Swarm constellation. *Earth, Planets, and Space*, 68, 121. <https://doi.org/10.1186/s40623-016-0502-5>
- Xiong, C., Xu, J., Wu, K., & Yuan, W. (2018). Longitudinal thin structure of equatorial plasma depletions coincidentally observed by swarm constellation and all-sky imager. *Journal of Geophysical Research: Space Physics*, 123, 1593–1602. <https://doi.org/10.1002/2017JA025091>
- Yizengaw, E., & Groves, K. M. (2018). Longitudinal and seasonal variability of equatorial ionospheric irregularities and electrodynamics. *Space Weather*, 16, 946–968. <https://doi.org/10.1029/2018SW001980>
- Yizengaw, E., Moldwin, M. B., Zesta, E., Biouele, C. M., Damtie, B., Mebrahtu, A., et al. (2014). The longitudinal variability of equatorial electrojet and vertical drift velocity in the African and American sectors. *Annales Geophysicae*, 32, 231–238. <https://doi.org/10.5194/angeo-32-231-2014>
- Yizengaw, E., Retterer, J., Pacheco, E. E., Roddy, P., Groves, K., Caton, R., & Baki, P. (2013). Postmidnight bubbles and scintillations in the quiet-time June solstice. *Geophysical Research Letters*, 40, 5592–5597. <https://doi.org/10.1002/2013GL058307>
- Yokoyama, T., & Fukao, S. (2006). Upwelling backscatter plumes in growth phase of equatorial spread F observed with the Equatorial Atmosphere Radar. *Geophysical Research Letters*, 33, L08104. <https://doi.org/10.1029/2006GL025680>
- Yokoyama, T., Pfaff, R. F., Roddy, P. A., Yamamoto, M., & Otsuka, Y. (2011). On postmidnight low-latitude ionospheric irregularities during solar minimum: 2. C/NOFS observations and comparisons with the Equatorial Atmosphere Radar. *Journal of Geophysical Research*, 116, A11326. <https://doi.org/10.1029/2011JA016798>
- Yokoyama, T., Shinagawa, H., & Jin, H. (2014). Nonlinear growth, bifurcation, and pinching of equatorial plasma bubble simulated by three-dimensional high-resolution bubble model. *Journal of Geophysical Research: Space Physics*, 119, 10,474–10,482. <https://doi.org/10.1002/2014JA020708>
- Yu, T., Miyoshi, Y., Xia, C., Zuo, X., Yan, X., Yang, N., et al. (2018). Solar dependence of equatorial F region irregularities observed by COSMIC radio occultations. *Journal of Geophysical Research: Space Physics*, 123, 9775–9787. <https://doi.org/10.1029/2018JA025936>
- Zakharenkova, I., Astafyeva, E., & Cherniak, I. (2016). GPS and in situ Swarm observations of the equatorial plasma density irregularities in the topside ionosphere. *Earth, Planets, and Space*, 68, 120. <https://doi.org/10.1186/s40623-016-0490-5>